# On-chip tightly-confined guiding and splitting of surface acoustic waves using line defects in phononic crystals

Feng Gao[1,3,4*], Sarah Benchabane[2], Amine Bermak[3], Shurong Dong[4], Abdelkrim Khelif[2]

[1] ZJU-Hangzhou Global Scientific and Technological Innovation Center, Zhejiang University, Hangzhou, China
[2] Institut FEMTO-ST, CNRS, Université de Bourgogne Franche-Comté, F-25030 Besançon Cedex, France
[3] College of Science and Engineering, Hamad Bin Khalifa University, Doha, Qatar
[4] College of Information Science & Electronic Engineering, Zhejiang University, Hangzhou, China

* Corresponding author: Feng Gao (gao.feng@zju.edu.cn)

## Abstract

Phononic crystals (PnCs) exhibit acoustic properties that are not usually found in natural materials, which leads to the possibility of new device designs for the complex manipulation of acoustic waves. In this article, we report the construction of a micron-scale phononic waveguide obtained by managing line defects in a phononic crystal to achieve on-chip, tightly-confined guiding, bending, and splitting of surface acoustic waves (SAWs). The PnC is made of a square lattice of periodic nickel pillars lying atop a piezoelectric substrate. The PnC lattice constant, pillar diameter, and pillar height are set to 10 $\mu m$, 7.5 $\mu m$, and 3.2 $\mu m$, respectively, leading to a complete band gap centered at 195 MHz. Interdigitated transducers are monolithically integrated on the same substrate for SAW excitation. The guiding, bending, and splitting of surface waves in the phononic waveguide are experimentally observed through measurement of the out-of-plane displacement fields using a scanning optical heterodyne interferometer. The combination of destructive interference due to the Bragg band gap and the interaction of the propagating wave with the pillars located at the immediate waveguide vicinity results in a tight confinement of the elastic displacement field. The proposed phononic waveguides demonstrate the feasibility of precise local manipulation of SAW that is essential for emerging frontier applications, notably for phonon-based classical and quantum information processing.

KEYWORDS: *Phononic crystal, Surface acoustic wave, Phononic waveguide, Phononic bandgap*

# 1. Introduction

Surface acoustic wave (SAW) devices are widely used in a variety of applications including wireless telecommunications[1, 2], sensing[3-5], and microfluidics[6, 7]. Over the past few years, their scope of use has significantly expanded and SAWs are now considered as promising systems for condensed matter physics[8]. The operation of existing SAW devices is based on the manipulation of planar surface waves excited by interdigitated transducers (IDTs), which usually have acoustic apertures (beam width) more than ten times larger than the wavelength. In contrast, the localized manipulation of SAW at lateral scales close to the wavelength remains challenging. Breakthrough in this field would be a significant extension of SAW technologies and is essential for the development of emerging frontier applications such as phonon-based quantum information processing[9, 10].

Phononic waveguides play an important role in the localized manipulation of SAW. They are typically constructed by specifically arranging phononic crystals (PnCs), which are made of periodic cells and can prohibit SAW propagation by acoustic bandgaps[11-13]. The bandgaps can be formed by different mechanisms including local resonances or Bragg reflection[14]. PnCs can be implemented on different substrates with various lattice structures [11, 15-17]. A variety of unit cells have also been reported in the literature, such as cylindrical holes [11], cylinder pillars [12], annular holes [18], etc.

Most of the researches regarding phononic waveguides for surface waves have focused on theoretical predictions. Back in 2006, Sun and Wu theoretically analyzed the possibility of guiding surface waves through sharp bends in line-defect phononic waveguides[19]. Alternative strategies for SAW waveguiding based on metamaterials were later proposed, notably based on hollow-pillar cavity mode PnCs[20], defect resonators in annual hole PnCs[21], self-collimation effect in PnCs[22] or edge waves in topological PnCs[23, 24].

One of the earliest implementations of a phononic waveguide for SAW was achieved by managing line defects in phononic crystals made by periodic arrays of holes in a solid matrix[25]. A subsequent design demonstrated a phononic waveguide integrated with IDTs on a piezoelectric lithium niobate substrate[26]. However, only straight waveguiding was demonstrated, leaving arbitrary guiding to be explored. Fully functional waveguides for Lamb waves, a close analogy to surface waves, were however experimentally implemented in different forms including phononic waveguides[27, 28], suspended beam waveguides[29], and coupled-resonator elastic waveguides[30]. It is only recently that advances in the field demonstrated the possibility to achieve arbitrary guiding of surface waves. Fu *et al.* reported the guiding of surface waves in ridged ring resonators and proved the relevance of their structures for the implementation of phononic circuits[31]. Wang *et al.* demonstrated the first arbitrary phononic waveguide based on valley-locked surface waves in topological PnCs[32], although in this last case the lateral confinement is relatively weak as the wave field penetrates a few wavelengths into the adjacent PnCs.

In this article, we report a phononic waveguide that supports arbitrary local manipulation of tightly-confined surface waves including guiding, turning, and splitting. The phononic waveguide is constructed by line defects in a square-lattice PnC with unit cells made of nickel pillars deposited atop a lithium niobate substrate. The guiding effect is achieved through the optimization of pillar geometry, mode selection, and channel design. IDTs were also monolithically integrated on the waveguide chip for the excitation of planar surface waves that are then guided through the phononic waveguide. In contrast to topological phononic waveguides, the free surface in the channel of the line-defect waveguide provides an open interface allowing direct in-channel integration of physical systems that can take full advantage of tightly-confined SAWs. This feature, combined with the precise manipulation of the surface wave propagation, illustrates the versatility of line-defect phononic waveguides in emerging applications such as phonon-based classical and quantum information processing.

## 2. Results and Discussion

### 2.1 Configuration of the phononic waveguide

The phononic waveguide is constructed by introducing line defects in square-lattice PnCs fabricated on a 128° Y-cut lithium niobate substrate as shown by Fig. 1a. IDTs with a 10-$\mu m$ pitch ($\lambda = 20\ \mu m$) are integrated on the same substrate for SAW excitation. Fig. 1b shows a schematic diagram of the lattice unit cell. The lattice constant ($a$) is 10 $\mu m$. Each unit cell contains a cylindrical nickel pillar of 7-$\mu m$ diameter ($d_p$) and 3.2-$\mu m$ height ($h_p$). The pillar dimensions are chosen by finite element method (FEM) optimization of the waveguide performance. The

waveguide channel width ($d_c$) is defined as the edge-to-edge distance between the side pillars (Fig. 1a). A scanning electron microscope (SEM) image of the fabricated pillars is shown in Fig. 1c. The pillars are fabricated using an electroplating-based process, leading to a rounded top (Fig. 1c). The pillar height ranges from 3.2 $\mu m$ to 3.6 $\mu m$ for different devices across the wafer due to the non-uniformity of the used electroplating process. The pillar diameter (7.7 $\mu m$) is also slightly larger than the designed value. Fig. 1d shows an SEM image of a SAW splitter constructed using such phononic waveguides. The splitter converts the planar surface wave from the IDTs to a guided wave and splits it into two branches. Other configurations including straight waveguide and bending waveguide are also implemented (Fig. S1 of Supporting Information).
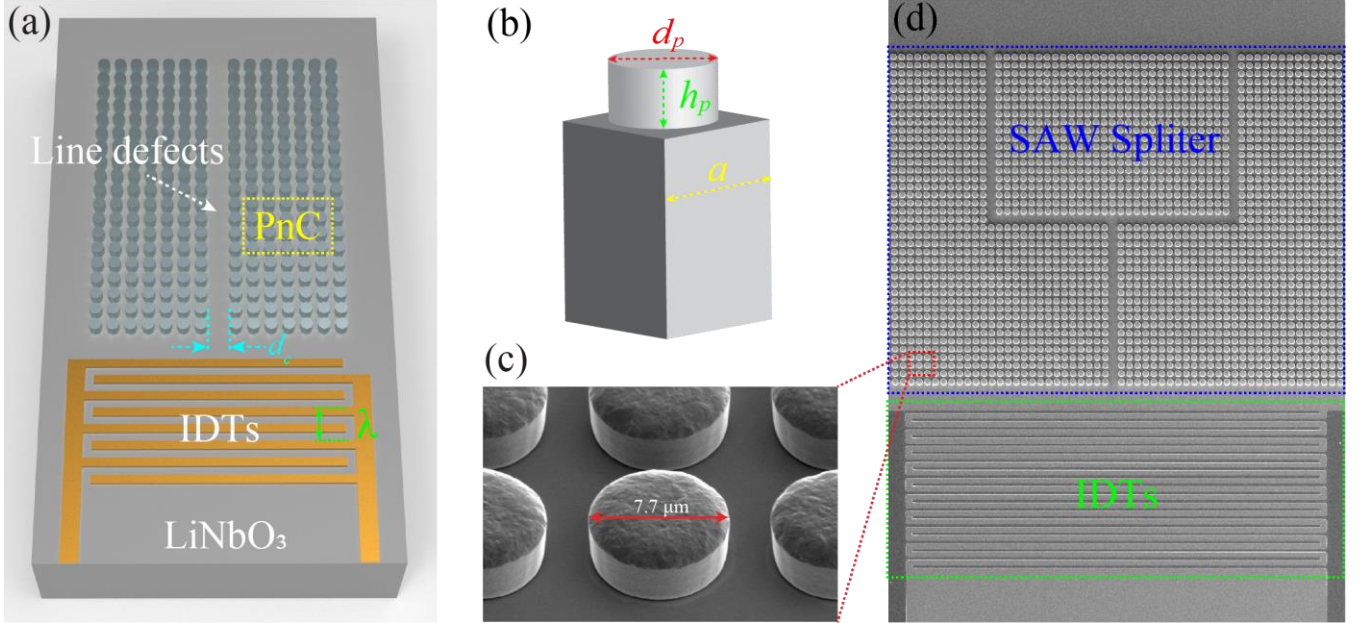


*Figure 1. (a) Schematic diagram of a straight waveguide formed by introducing line defects in a square lattice PnC. (b) Unit cell of the PnC with lattice constant a, pillar diameter $d_p$, and pillar height $h_p$. (c) Close-in image of the nickel cylinders in the PnC. (d) SEM image of the SAW splitter.*

## 2.2 Phononic bandgap for the prohibition of SAW propagation

A complete bandgap of the PnC is required to achieve the prohibition of SAW propagation in all directions. Fig. 2a shows the FEM simulated band structure of the PnC along the closed wave vector ($k$) path $\Gamma - X - M - Y$ in the first irreducible Brillouin zone (Fig. 2a insert). The wave vector lies on the surface plane with $k = X$ aligning with the X axis of the lithium niobate substrate. The $\Gamma - X - M - Y$ path contains complete wave propagation characteristics because of the substrate lattice symmetry. As the FEM eigenfrequency solver cannot distinguish bulk and surface modes, the data points of both modes are mixed in the band diagram. In order to highlight the band structure of surface waves, we modulated the transparency of the data point by the average displacement ratio between the surface and the bulk regions of the substrate. Opaque data points correspond to surface modes, while the data points with increasing transparency correspond to modes with higher bulk leakage. Pure bulk modes are removed in the band diagram as they are fully transparent. The FEM model and detailed data processing method are illustrated in Fig. S2 and Note I of Supporting Information. The blue region in Fig. 2a marks a complete Bragg bandgap where no surface waves can propagate in the PnC. Its lower boundary is determined by the surface mode frequency at the M point, which is 185.4 MHz. A vague upper boundary appeared around 213.2 MHz. The upper boundary is not explicit because it approaches the gradual transitioning regime of leaky modes and bulk modes. It should be noted that other data points with frequencies falling in the bandgap are leaky surface modes or bulk modes, which does not affect the complete prohibition of surface waves.

The transmission characteristic of a PnC block made of 10 pillars is shown in Fig. 2b. The simulation model is described in Fig. S3 and Note II of Supporting Information. Both the transmission along $k = X$ and $k = Y$ are simulated as shown by the blue and orange lines in Fig. 2b, respectively. The PnC bandgap is marked by the semi-transparent blue region. As expected, the transmission of surface modes in the bandgap frequency region is low.

The low transmission extends to the frequency regime above the bandgap due to the high bulk leakage in this regime. It can be noted that a small region below the bandgap also shows low transmission despite propagating modes existing in this region as shown by the violet data points in Fig. 2a. This is in fact because the violet data points correspond to breathing modes that cannot be excited by Rayleigh waves. Fig. 2c shows the mode shapes of the breathing mode and flexural modes at $k = Y$, which correspond to P1 and P2 marked by the black stars in Fig. 2a, respectively. In contrast to the flexural mode that shares similar motion with Rayleigh waves, the circular motion of the breathing mode is incompatible with the elliptical particle movement of Rayleigh waves. The lower boundary of the stopband is thus determined by the highest excitable surface modes (flexural modes) marked by the yellow data points in Fig. 2a, which are 164.5 MHz and 153.8 MHz for $k = X$ and $k = Y$, respectively. These two frequencies agree with the stop-band transition frequencies in Fig. 2b.

The effect of PnC on prohibiting SAW propagation is experimentally verified by measuring the out-of-plane z displacement using a scanning laser interferometer (Fig. S4). Fig. 2d shows the measured z displacement of a PnC in the propagation path of SAW excited by six pairs of IDTs (left side) at 200 MHz. The SAW amplitude represented by the measured z displacement is significantly reduced after passing through the PnC. Fig. 2e shows the frequency spectra of the SAW amplitudes before and after passing through the PnC block. The input (before PnC) and output (after PnC) amplitude sampling areas are marked by the red and green dashed rectangles in Fig. 2d, respectively. The input SAW reaches maximum amplitude at 195 MHz, which is determined by the IDT periodicity ($\lambda_0 = 20\mu m$) and the SAW velocity on the 128° Y-cut lithium niobate substrate ($v = 3894 \ m/s$). After passing the PnC block, the output SAW amplitude drops to the noise floor of the optical measurement setup due to the strong attenuation caused by the phononic bandgap.
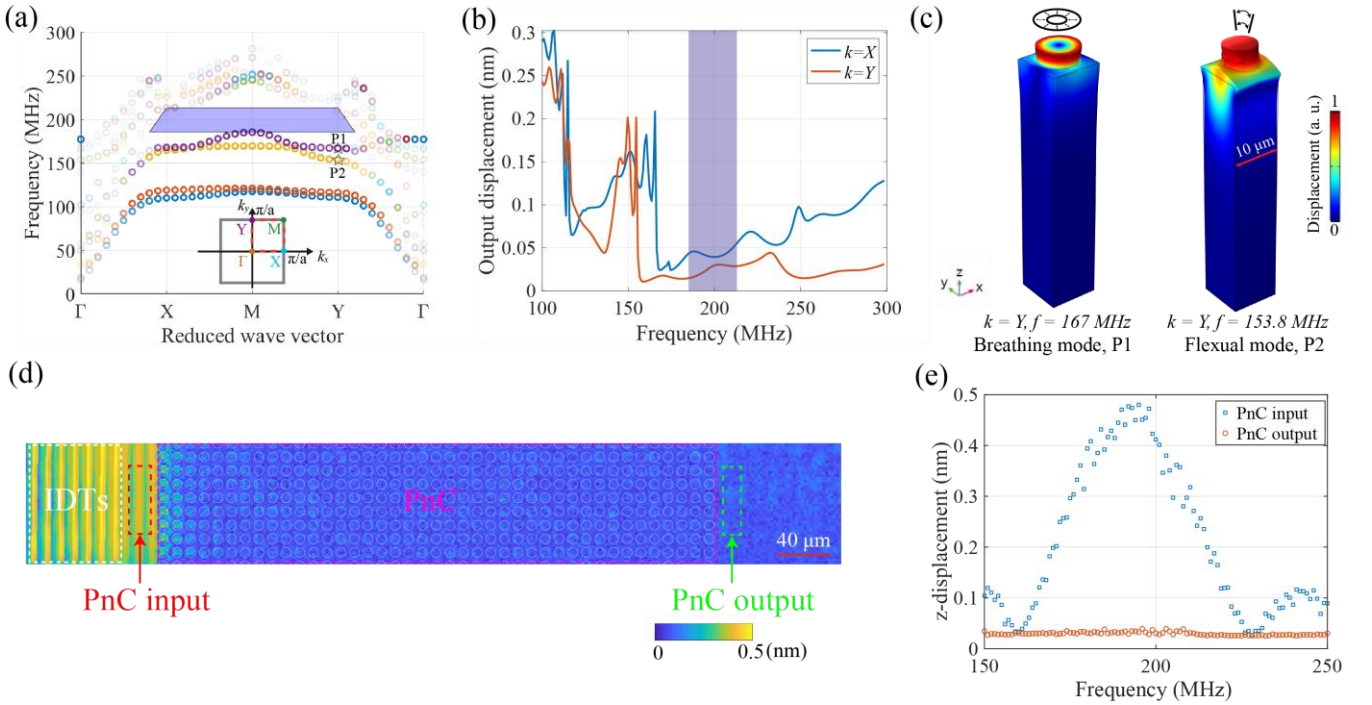


Figure 2. (a). Band structure of the PnC crystal made of a square lattice of nickel cylinder pillars. The blue region marks the complete SAW bandgap. Insert shows the corresponding first irreducible Brillouin zone used in the band structure. (b) The transmission spectra of a PnC block with 10-pillar depth. The bandgap regime marked by the blue region shows low transmission. (c). Mode shape of breathing and flexural modes at $k = Y$. (d) Measured out-of-plane z displacement map showing that the SAW is blocked by a PnC with 41-pillar depth. (e) z displacement spectra before and after the 41-pillar PnC.

## 2.3 Guided SAW characteristics in the line-defect channels

Guided SAW in the line-defect channels must be compatible with the mode constraints of the adjacent nickel pillars of the PnC to sustain its propagation. The elastic wave propagation properties in the phononic waveguide can thus vary drastically from the planar SAW. Fig. 3a shows the mode shape of the guided SAW ($f = 201 \ MHz$, $k = Y$) in

a single-row line-defect waveguide unit cell ($h_p = 3\mu m$, $d_p = 7\ \mu m$, see Fig. S5 and Note III of Supporting Information for FEM model description). Its displacement field is mostly confined in the center of the line-defect channel near the surface region. The out-of-plane displacements along X and Z cutlines (white-dashed line in Fig. 3b) confirm that the wave amplitude decreases quickly away from the channel center and surface, respectively. The tight lateral confinement is due to the strong Bragg reflection of the PnCs. The off-resonance flexural vibration of the pillars located close to the line-defect channel also stores part of the elastic energy and enhances the Bragg reflection. The wave velocity inside the channel waveguide was found equal to $\square_{\square\square\square} = \square \times \square = 4020\ \square/\square$. This velocity is higher than the shear bulk acoustic wave (S-BAW, slowest bulk wave) velocity $\square_{\square-\square\square\square} = 3700\ \square/\square$. In principle, surface waves with a velocity higher than the S-BAW will be leaky waves. It was however previously reported that PnCs allow SAW modes to propagate at velocities higher than the radiation limit[33]. The higher velocity observed in the present phononic waveguide is a similar effect and could be possibly attributed to the existence of bound states in the continuum (BIC) modes that allow propagation above the radiation limit due to the localized confinement of wave energy by the periodic pillars[34].
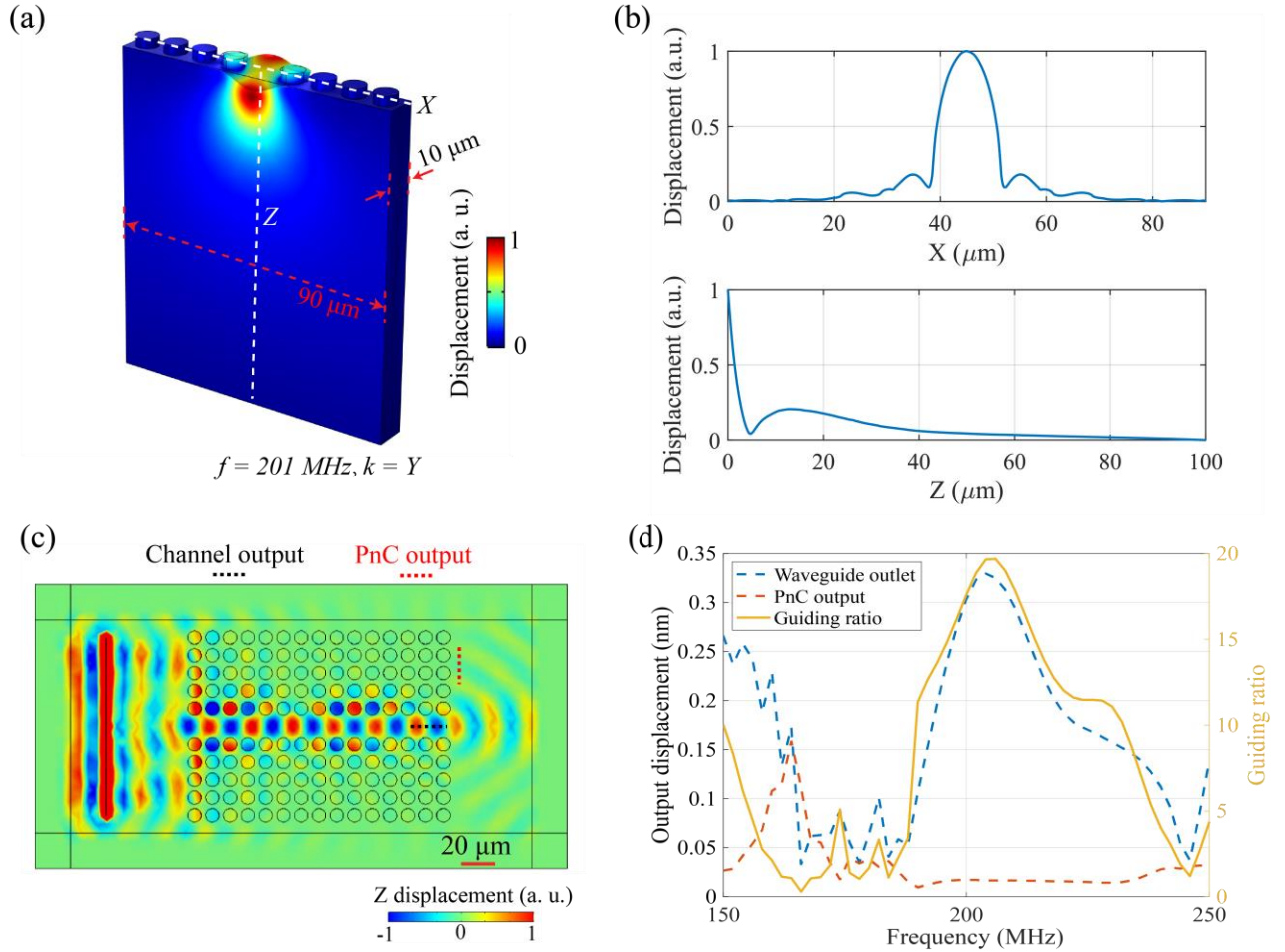


*Figure 3. (a). Mode shape of a waveguide unit cell showing the tight confinement of the displacement field. (b) The out-of-plane z displacements along X and Z cutlines show that the displacement decreases quickly away from the waveguide center and the surface. (c) Displacement map of a straight waveguide ($h_p = 3\ \mu m$, $d_p = 7\ \mu m$) at 200 MHz excitation showing the guided SAW along the channel and a diffraction pattern at the outlet. (d). The frequency characteristics of the straight waveguide. A transmission peak is observed at 204 MHz.*

Fig. 3c shows the simulated z displacement map of a straight waveguide formed by a single row of line defect ($h_p = 3\ \mu m$, $d_p = 7\ \mu m$, see Fig. S6 and Note IV of Supporting Information for FEM model description). The waveguide channel aligns with the X axis of the LiNbO₃ substrate. A line source on the left side of the model oscillates in the Z direction to excite the surface waves. As shown by the displacement map, the planar SAW entering the PnCs on the upper and lower side of the model is quickly attenuated. As a result, the vibration amplitude of the pillars also decreases quickly along the SAW propagation direction. In contrast, the line-defect channel in

5

the center allows the propagation of a guided surface mode. At the outlet of the channel, a circular diffraction pattern can be observed, which is because the output is a point source of surface waves. It can also be observed that the lateral penetration of the SAW displacement field into the PnC varies along the channel and exhibits a sinusoidal pattern. This pattern originates from the formation of standing waves caused by the in-channel reflections.

The frequency characteristics of the straight waveguide are obtained by sweeping the oscillation frequency of the line source. The mean z displacement amplitude at the end of the waveguide channel ($\bar{u}_{wg}$, black dashed line in Fig. 3c) and after the PnC ($\bar{u}_{PnC}$, red dashed line in Fig. 3c) are extracted to compare the transmission through the line defect channel and the PnC, respectively. The ratio between the two displacements is defined as the guiding ratio ($G = \bar{u}_{wg}/\bar{u}_{PnC}$) for evaluating the effectiveness of the waveguide. A large guiding ratio means that SAW is mostly transmitted through the line-defect channel with little leakage through the PnC. The frequency spectra of $\bar{u}_{wg}$, $\bar{u}_{PnC}$ and G are shown by the blue dashed line, orange dashed line, and yellow solid line in Fig. 3d, respectively. Low transmission through the PnC ($\bar{u}_{PnC}$) is observed from 174 MHz to 250 MHz due to the existence of the phononic bandgap. The transmission through the line-defect channel ($\bar{u}_{wg}$) is maximum at 204 MHz with a 3-dB passband between 195.7 to 215 MHz. The guiding ratio spectrum around the passband follows the trend of the channel transmission spectrum as the PnC transmission remains flat in this regime.

## 2.4 Parametric optimization of the line-defect SAW waveguide

To optimize the performance of the phononic waveguide, parametric sweeping of its design parameters including pillar diameter, pillar height, and channel width is performed. Fig. 4a shows the guiding ratio (yellow line) of the straight waveguide when the pillar diameter varies from 1 to 10 $\mu m$. The pillar height is fixed at 3 $\mu m$ for the sweeping. Results show that the guiding ratio reaches its maximum at 7-$\mu m$ pillar diameter. Based on this optimum pillar diameter, a sweeping of pillar height from 1 to 10 $\mu m$ is then performed. Fig. 4b shows that the guiding ratio has two peaks at 3.2 $\mu m$ and 5.4 $\mu m$. The valley of the guiding ratio between the two peaks is mainly caused by the increase of wave leakage through the PnC (Orange-dashed line in Fig. 4b). Despite both guiding ratio peaks exhibiting high guiding effectiveness, it was found that only the pillar heights in the range of 2.6 to 3.8 $\mu m$ support SAW bending and splitting. This is because pillars with a height around 3.2 $\mu m$ have elliptical flexural mode polarizations (Fig. 4c upper part) that are compatible with both the waves propagating in the inlet channel and split channels. In contrast, the pillars with heights around 5.4 $\mu m$ show a linear flexural mode polarization (Fig. 4c lower part) that aligns with the wave propagation, which cannot be converted to polarization in the perpendicular direction and thus does not support wave bending.

Fig. 4d shows the guiding ratio of the straight waveguide at different channel widths. The wave is completely blocked when the channel width is smaller than 10 $\mu m$ (half a wavelength), leading to a low guiding ratio. It then increases with the increase of channel width and reaches a stable value. In contrast to the straight waveguide that can have arbitrary channel widths, the channel width of a bending waveguide needs to be multiple of the lattice constant to keep the pillars aligned with the lattice around the turning corner. Fig. 4e and Fig. 4f show the simulated propagation of guided SAW through 90°-bending waveguides with 1-pillar and 2-pillar line defects, respectively. The results show that SAW can be guided through the 1-pillar line-defect bending, while the guided SAW turns into an asymmetric mode and attenuates quickly after passing the 2-pillar bending. A similar phenomenon is observed in SAW splitters with 1-pillar and 2-pillar line-defect channels (Fig. S7 of Supporting Information). It is thus necessary to use 1-pillar line-defect channels to support bending and splitting in the phononic waveguide. Besides the impact on transmission, channel width also affects the bandwidth of the waveguide. The outlet displacement spectra of three straight waveguides with 1-pillar, 2-pillar, and 3-pillar line-defect channels show 3-dB bandwidths of 19.3 MHz, 27.3 MHz, and 27.5 MHz, respectively (Fig. S8 of Supporting Information). The larger bandwidths of the 2-pillar and 3-pillar line-defect waveguides can be attributed to the lessened restriction from the adjacent PnCs on the guided elastic wave at larger channel widths. Fig. S8 also shows the passband center frequencies of the 2-pillar and 3-pillar waveguides shift down compared to the 1-pillar waveguide, which points to a reduction in propagation velocity. This is also caused by the reduced mode restriction from the PnC at increased channel width, resulting in a gradual transition from the BIC mode to a regular Rayleigh mode.
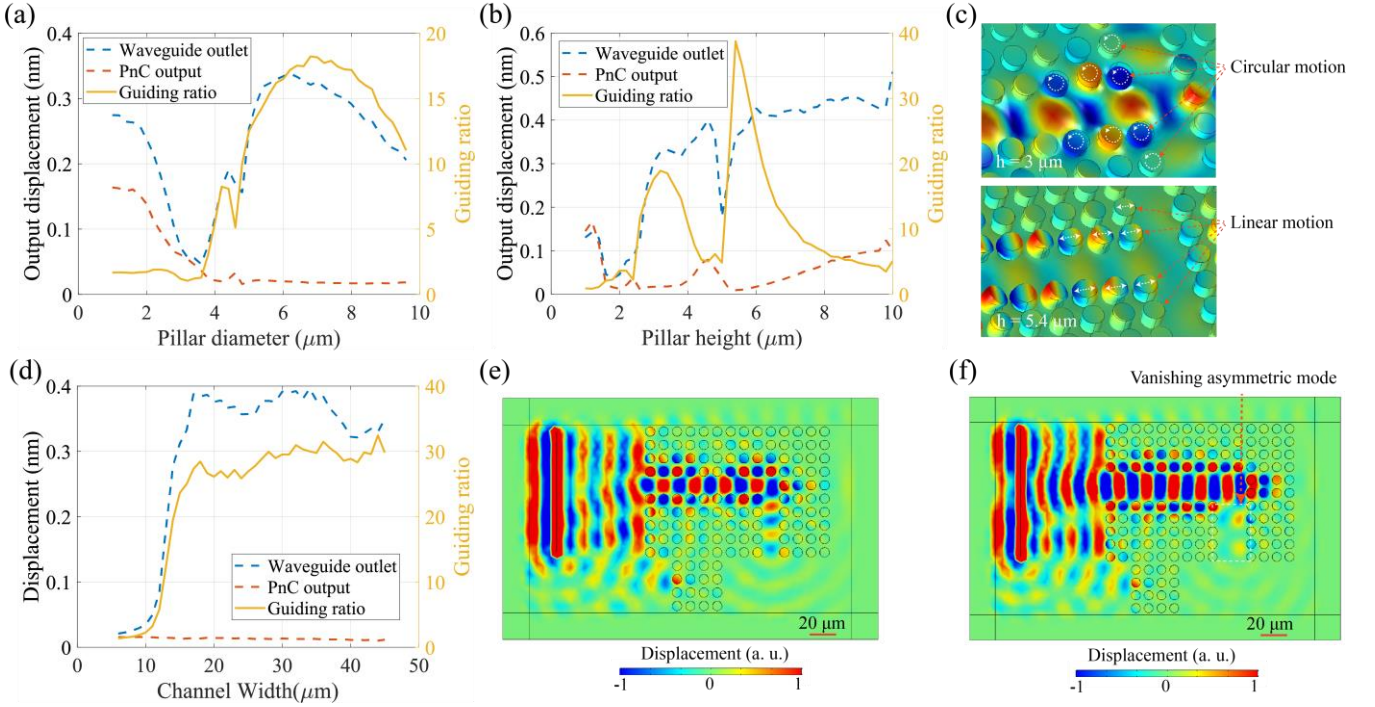
*Figure 4. (a) Pillar diameter sweep showing a peak guiding ratio at $d_p = 7\ \mu m$. (b) Pillar height sweep showing that both $h_p = 3.2\ \mu m$ and $h_p = 5.4\ \mu m$ offers good guiding effectiveness. (c) Pillar heights around $3\ \mu m$ can support SAW bending due to the circular motion of the pillars (upper figure) while pillar heights around $5.4\ \mu m$ do not allow SAW bending due to the linear pillar motion. (d) The guiding ratio starts to increase when the channel width is greater than $10\ \mu m$ and saturates when it is greater than $15\ \mu m$. (e). 1-pillar line-defect channel can support SAW bending (f). 2-pillar line defect channel does not allow SAW bending because of the excitation of asymmetric mode after the bend.*

## 2.5 Experimental characterization of the waveguide

Based on the optimized design parameters obtained by FEM, straight, 90°-bending and SAW splitter waveguides with 1-pillar line-defect channels were implemented. Out-of-plane z displacements of the three waveguides (Fig.5a-Fig.5c) were measured to visualize the guided SAW propagation. To highlight the line-defect channels, the PnCs in each of the waveguides are covered by light-gray overlays with white-dashed line borders. IDTs on the left of the waveguides are used to excite the planar surface waves. The straight waveguide (Fig. 5a) demonstrates clear confinement and guiding of SAW along the line-defect channel. A diffraction pattern can be observed at the outlet of the waveguide, which agrees well with the simulation result in Fig. 3c. Measurement of the 90°-bending waveguide (Fig. 5b) shows the guided surface wave can be turned twice in the line-defect channel and still produces a diffraction pattern at the outlet. Nevertheless, a relatively large attenuation is observed at the turning corners of the waveguide. The outlet diffraction pattern is also less regular than that of the straight waveguide, which is due to the disturbance of the leaked SAW from the PnC region. The z displacement map of the SAW splitter in Fig. 5c demonstrates the dividing of SAW into two branches. The splitter is symmetric along the input channel. Zoomed images of the splitting point and upper outlet of the splitter are shown in the lower part of Fig. 5c. Similar to the 90°-bending waveguide, strong attenuation is observed at the splitting/bending corners. The diffraction pattern at the output is also distorted due to the interference by the SAW leaked directly from the PnC.

Fig. 5d shows the out-of-plane z displacement amplitudes of SAW along the center of the straight waveguide from the inlet to the outlet. The amplitude curves exhibit standing wave ripples due to the internal reflection in the waveguide channel. Linear fittings of the two curves are used to extract the guided SAW attenuation rate. It should be noted that this attenuation pertains to the z displacement component, as the laser interferometer can only measure out-of-plane vibrations. Fig. 5e shows the spectrum of the z displacement attenuation rate, which increases with the excitation frequency. The measured frequency range is from 190 MHz to 200 MHz due to the limitation of the IDT excitation bandwidth and the displacement measurement noise level of the interferometer. Simulation of the in-channel displacement components of a 1-pillar line-defect straight waveguide at 194 MHz (Fig. S9) revealed similar

attenuation rates for the in-plane x (parallel to propagation direction) and out-of-plane z displacement amplitudes, which can be accounted for by the fact that they constitute the two major components of the guided mode. In contrast, the in-plane y (perpendicular to propagation direction) displacement component is much smaller than the x and z components and exhibits a different attenuation trend, which is possibly due to the y component mainly stemming from the vibration of adjacent pillars rather than from the guided wave.
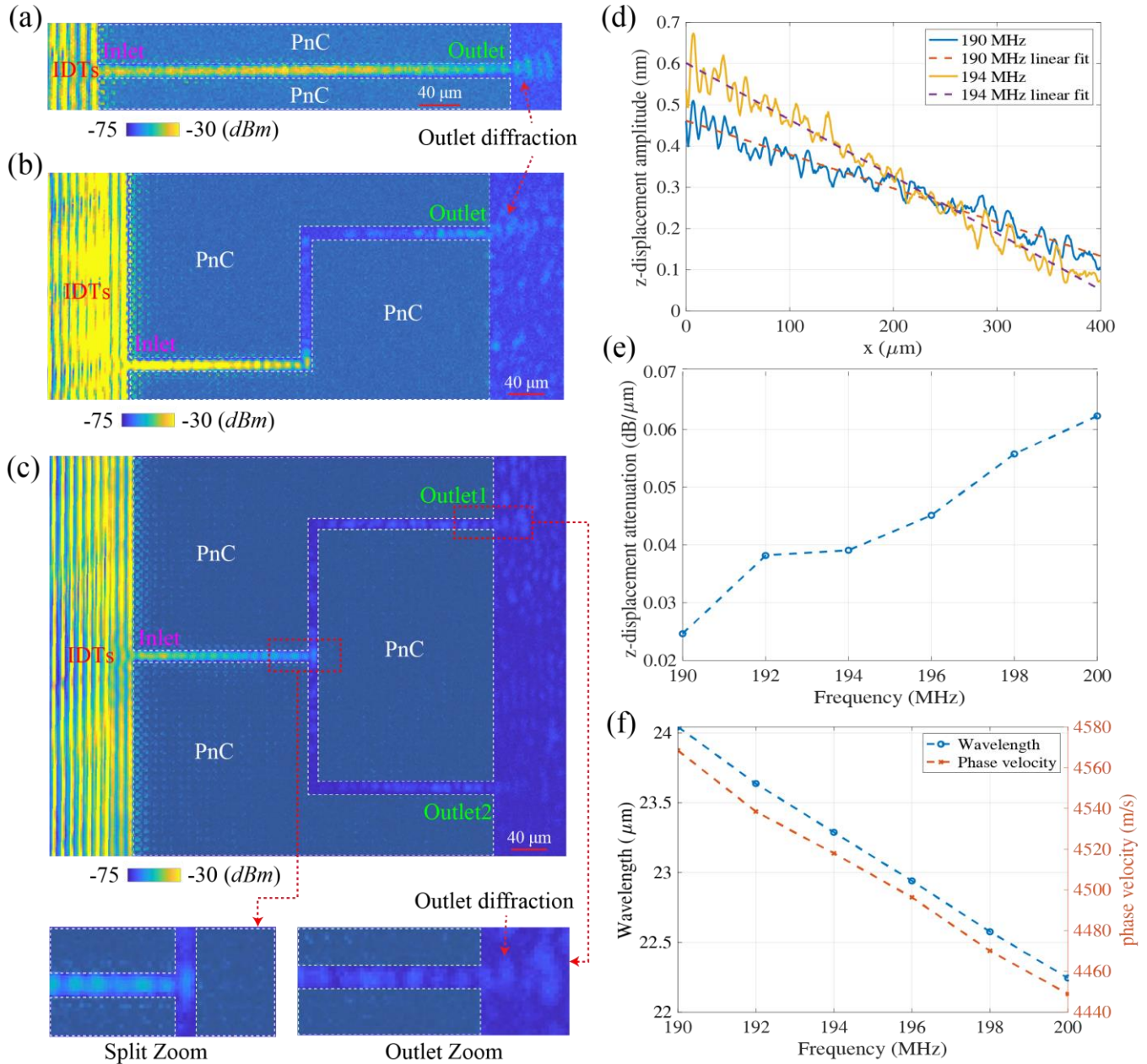


*Figure 5. Out-of-plane z displacement of (a) Straight waveguide (b) 90°-bending waveguide and (c) SAW Splitter (d). SAW z displacement amplitude along the center of the straight waveguide at 190 and 194 MHz. (e). SAW z displacement attenuation rate in the straight waveguide from 190 MHz to 200 MHz. (f). SAW wavelength and phase velocity in the straight waveguide channel from 190 MHz to 200 MHz.*

To obtain the wavelength and phase velocity, we also measured the SAW phase variation in the straight waveguide channel. The measured SAW waveform and phase data are given in Fig. S10 of Supporting Information. Fig. 5f shows the wavelength and phase velocity of the guided SAW in the straight waveguide. The measured SAW wavelength (23.1 $\mu m$ at 195 MHz) in the waveguide is longer than the Rayleigh SAW wavelength on the free surface (20.4 $\mu m$ at 195 MHz). This means that the guided SAW has a higher velocity than the Rayleigh SAW and suggests that the guided SAW is a BIC mode. The phase velocity decreases from 4568 m/s at 190 MHz to 4449 m/s at 200 MHz. The group velocity is 2986 m/s, which is derived from the slope of the wavelength vs frequency curve. The

measured guided SAW wavelength and phase velocity show similar trends as the simulation results (Fig. S11), despite the latter having slightly higher values ($\lambda = 24.1 \ \mu m$ simulated vs $\lambda = 23.1 \ \mu m$ measured at 195 MHz). This discrepancy could be attributed to the pillar profile and nickel material property difference between simulation and experimental implementation.

The decreasing phase velocity in Fig. 5f implies the reduction of SAW radiation loss to the bulk at higher frequencies, which in turn should result in a reduction of the propagation attenuation. However, the measured attenuation increases with increasing excitation frequency, which means that leakage to the bulk is not the limiting factor for attenuation. This agrees with the simulation result in Fig. 3a, which shows a non-leaking guided mode with higher phase velocity than the S-BAW.

## 2.6 Discussion

The proposed phononic waveguides rely on the local confinement of SAW in PnC line defects utilizing the complete bandgap of the PnC. In fact, the lower boundary of the complete bandgap (Fig. 2a) is defined by the highest propagating surface mode, while the upper band gap exit is set by the radiation limit determined by the S-BAW. Due to the presence of the periodic nickel pillars, this radiation limit is higher than the S-BAW velocity. The guided SAW in the phononic waveguide also exhibits a higher velocity than the S-BAW, which suggests that the guided mode should be leaky. Nevertheless, the simulation result in Fig. 3a shows that it is a perfectly confined non-leaky mode. This phenomenon is possibly due to the guided mode being a symmetry-protected BIC mode that is preserved by the periodicity of the PnC pillars[34].

The waveguide performance is described by its guiding ratio, which is determined by the pillar height, pillar diameter, and channel width. First, the increase of pillar diameter increases the reflection from each individual cell and thus improves the guiding ratio. However, the guiding ratio drops when the pillar diameter exceeds $7 \ \mu m$. As the transmission through the PnC remains low when the pillar diameter is over $4 \ \mu m$, the guiding ratio decrease is mainly caused by a decrease in the waveguide channel transmission, which could be due to increased elastic dissipation of the pillars at larger diameters. Second, the guiding ratio vs pillar height curve shows two local optimums at $3.2 \ \mu m$ and $5.4 \ \mu m$. However, the pillars with heights around $5.4 \ \mu m$ exhibit linear flexural mode polarization that does not support the turning of SAW. Conversely, the elliptical flexural mode polarization of the pillars around $3.2 \ \mu m$ high can seamlessly transit to the perpendicular channel and thus supports SAW turning. Third, the channel width controls the SAW mode in the waveguide. When the channel is made of a single row of line defects, a symmetric mode propagates in the waveguide and can pass through the 90°-bend. In contrast, the guided SAW passing through the 2-pillar 90°-bend transforms to an asymmetric mode that attenuates quickly. It is thus necessary to construct the waveguide with 1-pillar line defects.

Although on-chip SAW waveguiding has been successfully demonstrated, the proposed waveguide still exhibits relatively high attenuation that should be addressed in the future. One major factor of attenuation is the backscattering along the waveguide. This effect can be reduced by optimizing the geometries of the pillars along the channel in order to reach a good trade-off between channel attenuation and lateral confinement. Another factor of attenuation lies at bends and intersections, which involve both backscattering and leakage into the PnC. One possible solution to alleviate this issue is to use a different lattice type such as triangular lattice or hexagonal lattice that can support different turning angles from the 90° angle imposed by the rectangular lattice. The unit cell geometry can also play an important role in guiding performance as it affects the internal reflection and polarization. Assigning pillars with different geometries to the turning corners such as triangular pillars or elliptical pillars that tend to polarize in selected directions can possibly reduce the bending attenuation. It is also possible to introduce a different type of waveguide in the PnC corners for bending loss reduction. This waveguide can be a topological waveguide[31, 32] or a phononic waveguide with a different lattice cell, although such a reduction in bending loss may occur at the expense of lateral confinement. Integration with a line-defect waveguide can be implemented through gradually transitioning lattice cells or through tapered waveguides that have varying channel widths[35]. Moreover, further optimization of the substrate crystal orientation can also help reduce the attenuation. Besides improving the attenuation, using tapered waveguides between the IDTs and the line-defect inlet/outlet can help reduce the wave energy propagation in the PnC area and thus increase the impinging SAW coupling efficiency.

## 3. Conclusion

In summary, we developed a micron-scale phononic waveguide for the on-chip guiding, bending, and splitting of surface acoustic waves. The phononic waveguide is constructed by introducing line defects in phononic crystals made of square lattices of nickel pillars. The waveguide achieved tight lateral confinement due to the strong lateral Bragg reflection. Although the velocity of the guided mode is found to be higher than that of the Rayleigh wave on the free surface, it is still a non-leaky mode with most of the displacement field confined near the surface, possibly due to the formation of a BIC mode. Optimum design parameters including pillar diameter, pillar height, and channel width of the waveguides are obtained through finite element analysis. The waveguides were experimentally implemented on a 128° Y-cut lithium niobate substrate with monolithically integrated IDTs. The guiding effects were experimentally characterized and visualized by measurement of its out-of-plane displacement field using a scanning optical heterodyne interferometer. This phononic waveguide demonstrates the feasibility of arbitrary on-chip manipulation of SAWs while achieving tight lateral confinement within a single wavelength. It can serve as an enabling technology for future applications that requires precise local manipulation of acoustic energy or phonons such as classical and quantum information processing or sensing.


## 4. Experimental Section

*Simulation setup:* The FEM modeling of the PnC and the waveguide was performed with COMSOL Multiphysics®. Solid mechanics, electrostatics, and piezoelectric effects were solved for the geometry. The band diagram was obtained by eigenfrequency simulations. The simulation model is given in Fig. S2 of Supporting Information. The depth of the substrate was set to five lattice constants (50 $\mu m$) with a fixed boundary condition applied to the bottom. Floquet boundary conditions were applied to the front-back sides and left-right sides of the unit cell. In the Floquet boundary condition, $k_x$ and $k_y$ were set to sweep across the first irreducible Brillouin zone ($\Gamma - X - M - Y$), while $k_z$ was set to zero. The bulk modes and leaky modes were then filtered out by lowering their data point transparency. The mode shape of the unit-cell waveguide is also obtained by eigenfrequency study with the model shown in Fig. S5 of Supporting Information.

The PnC transmission characteristics were simulated using a simplified one-column model shown in Fig. S3 of Supporting Information. Frequency domain simulation was used to resolve the displacement values from 100 MHz to 300 MHz. A line source with 1-nm prescribed displacement along Z axis was used to generate the SAW. The out-of-plane z displacement after 10 pillars is used to evaluate the transmission from the PnC. PMLs were added to the two ends of the geometrical model along the propagation axis to remove boundary reflection. Periodic boundary conditions were applied to the two sides parallel to the propagation axis, which effectively extends the column number to infinity. The depth of the model is 100 $\mu m$ with a fixed boundary condition applied to the bottom.

The simulation of the straight waveguide, 90°-bending waveguide, and SAW splitter were all performed in the frequency domain study. The simulation model is shown in Fig. S6 of Supporting Information. A line source with 1-nm prescribed displacement was used for SAW generation. The z displacement at the output of the waveguides was used to evaluate their transmission characteristics. PMLs were added to the surrounding of the geometrical models to remove the reflection. The substrate depth is set to 60 $\mu m$ with a fixed boundary condition applied to the bottom.

*Device fabrication:* The waveguides were fabricated using an electroplating-based process. The process flow chart is given in Fig. S12 of Supporting Information. After cleaning with piranha solution, 15-nm titanium and 100-nm copper were deposited on the 4-inch 128° Y-cut lithium niobate substrate. The copper layer was used as the seed layer for nickel electroplating while the titanium layer was used to promote the adhesion of copper to the lithium niobate substrate. A complementary photoresist pattern (AZ9260, 6 $\mu m$ thick) of the phononic crystal pillars was then added to the substrate by optical lithography. The photoresist pattern was used as the electroplating mold. Nickel electroplating is then performed at a current of 0.2A for 35 minutes. The thickness of the electroplated nickel ranges from 3.2-3.6 $\mu m$ across the wafer due to the process variation. The photoresist is then removed by immersing the wafer in Microposit 1165 remover at $70°C$ for 30 minutes. Reactive ion etching (RIE) is then used to remove the copper and titanium layers on the blank region. Subsequently, IDTs were fabricated by a lift-off process. The complementary photoresist pattern (AZ nLof 2020, 3 $\mu m$) of the IDTs was first added to the wafer. E-beam evaporation is then used to deposit 10-nm titanium and 200-nm aluminum on the wafer. The wafer is then immersed in

70°C Mic. Microposit 1165 photoresist remover overnight to complete the lift-off process. The individual waveguide devices are then diced from the wafer using a mechanical dicing saw.

*Measurement of out-of-plane z displacement:* A laser scanning heterodyne interferometer was used to measure the z displacement in the waveguides. The interferometer is in a Mach-Zehnder configuration as shown in Fig. S4 of Supporting Information. The output of a 633-nm laser (Thorlabs HRS015B) is split into two frequency-shifted beams by an acousto-optic modulator (AA Opto Electronic MTS110-A3-VIS). The two beams are orthogonally polarized. The frequency-shifted beam is used as the reference beam and goes directly to the photodiode detector after passing through reflecting mirrors and a polarizing beam splitter (PBS). The other beam without frequency shift is used as the signal beam that goes to the device surface. It is focused on the device surface by a long-working distance microscope objective with a numerical aperture of 0.8 (Olympus LMPLFLN100x). The laser spot size on the device is about 650 nm. The reflected signal beam from the device surface recombines with the reference beam through the PBS. The phase of the signal beam is modulated by the z displacement of the device. The interference of the two beams is detected by a fast photodiode (Alphalas UPD-200-SP). The photodiode signal is amplified and detected by either a spectrum analyzer (Anritsu MS2830A) for obtaining the displacement amplitude or an oscilloscope (Agilent DSO9254A) for acquiring the displacement phase maps. The device is wire bonded to a printed circuit board (PCB) and connected to a signal synthesizer (Agilent N5181A) for SAW excitation. The scanning is implemented by mounting the PCB on a nano-positioning stage (Aerotech ANT95XY). The 2D displacement map is obtained by driving the stage to scan across the designated device area with 1.5 $\mu m$ steps and measuring the displacement at each point.

## Supporting Information
Supporting Information is available from the Wiley Online Library or from the author.

## Conflict of interest
The authors declare no conflict of interest.

## Author contributions
Feng Gao, Amine Bermak, Sarah Benchabane, and Abdelkrim Khelif proposed the idea. Feng Gao and Sarah Benchabane designed the fabrication process and the characterization method. Feng Gao fabricated and tested the device. Feng Gao, Abdelkrim Khelif, Sarah Benchabane, and Shurong Dong drafted the manuscript.

## Data Available Statement
The data that support the findings in this study are available from the corresponding author upon request.

## Reference

1. R. Su, J. Shen, Z. Lu, H. Xu, Q. Niu, Z. Xu *et al.*, Wideband and low-loss surface acoustic wave filter based on 15° YX-LiNbO₃/SiO₂/Si structure. *IEEE Electron Device Lett.* **2021**, 42, 438-441.
2. J. Shen, S. Fu, R. Su, H. Xu, Z. Lu, Z. Xu *et al.*, High-performance surface acoustic wave devices using LiNbO 3/SiO 2/SiC multilayered substrates. *IEEE Trans. Microw. Theory Tech.* **2021**, 69, 3693-3705.
3. M. Agostini, F. Lunardelli, M. Gagliardi, A. Miranda, L. Lamanna, A. G. Luminare *et al.*, Surface‐Acoustic‐Wave (SAW) Induced Mixing Enhances the Detection of Viruses: Application to Measles Sensing in Whole Human Saliva with a SAW Lab‐On‐a‐Chip. *Adv. Funct. Mater.* **2022**, 32, 2201958.

4. F. Gao, F. Boussaid, W. Xuan, C.-Y. Tsui, A. Bermak, Dual transduction surface acoustic wave gas sensor for VOC discrimination. *IEEE Electron Device Lett.* **2018**, 39, 1920-1923.

5. F. Gao, A. Bermak, S. Benchabane, L. Robert, A. Khelif, Acoustic radiation-free surface phononic crystal resonator for in-liquid low-noise gravimetric detection. *Microsyst. Nanoeng.* **2021**, 7, 8.

6. R. J. Shilton, V. Mattoli, M. Travagliati, M. Agostini, A. Desii, F. Beltram *et al.*, Rapid and Controllable Digital Microfluidic Heating by Surface Acoustic Waves. *Adv. Funct. Mater.* **2015**, 25, 5895-5901.

7. M. Wu, Z. Mao, K. Chen, H. Bachman, Y. Chen, J. Rufo *et al.*, Acoustic separation of nanoparticles in continuous flow. *Adv. Funct. Mater.* **2017**, 27, 1606039.

8. P. Delsing, A. N. Cleland, M. J. Schuetz, J. Knörzer, G. Giedke, J. I. Cirac *et al.*, The 2019 surface acoustic waves roadmap. *J. Phys. D: Appl. Phys.* **2019**, 52, 353001.

9. K. J. Satzinger, Y. Zhong, H.-S. Chang, G. A. Peairs, A. Bienfait, M.-H. Chou *et al.*, Quantum control of surface acoustic-wave phonons. *Nature* **2018**, 563, 661-665.

10. R. Manenti, M. Peterer, A. Nersisyan, E. Magnusson, A. Patterson, P. Leek, Surface acoustic wave resonators in the quantum regime. *Phys. Rev. B.* **2016**, 93, 041411.

11. V. Laude, M. Wilm, S. Benchabane, A. Khelif, Full band gap for surface acoustic waves in a piezoelectric phononic crystal. *Phys. Rev. E.* **2005**, 71, 036607.

12. A. Khelif, Y. Achaoui, S. Benchabane, V. Laude, B. Aoubiza, Locally resonant surface acoustic wave band gaps in a two-dimensional phononic crystal of pillars on a surface. *Phys. Rev. B.* **2010**, 81, 214303.

13. M. Oudich, N. J. Gerard, Y. Deng, Y. Jing, Tailoring Structure-Borne Sound through Bandgap Engineering in Phononic Crystals and Metamaterials: A Comprehensive Review. *Adv. Funct. Mater.* **2022**, 2206309.

14. D. Zhang, J. Zhao, B. Bonello, F. Zhang, W. Yuan, Y. Pan *et al.*, Investigation of surface acoustic wave propagation in composite pillar based phononic crystals within both local resonance and Bragg scattering mechanism regimes. *J. Phys. D: Appl. Phys.* **2017**, 50, 435602.

15. S.-Y. Yu, J.-Q. Wang, X.-C. Sun, F.-K. Liu, C. He, H.-H. Xu *et al.*, Slow surface acoustic waves via lattice optimization of a phononic crystal on a chip. *Phys. Rev. Appl.* **2020**, 14, 064008.

16. S.-Y. Yu, X.-C. Sun, X. Ni, Q. Wang, X.-J. Yan, C. He *et al.*, Surface phononic graphene. *Nat. Mater.* **2016**, 15, 1243-1247.

17. S. Mohammadi, A. Khelif, R. Westafer, E. Massey, W. D. Hunt, A. Adibi, Full band-gap silicon phononic crystals for surface acoustic waves, *ASME International Mechanical Engineering Congress and Exposition*, **2006**.

18. B. Ash, S. Worsfold, P. Vukusic, G. Nash, A highly attenuating and frequency tailorable annular hole phononic crystal for surface acoustic waves. *Nat. Commun.* **2017**, 8, 1-7.

19. J.-H. Sun, T.-T. Wu, Propagation of surface acoustic waves through sharply bent two-dimensional phononic crystal waveguides using a finite-difference time-domain method. *Phys. Rev. B.* **2006**, 74, 174305.

20. Muhammad, C. Lim, J. Reddy, E. Carrera, X. Xu, Z. Zhou, Surface elastic waves whispering gallery modes based subwavelength tunable waveguide and cavity modes of the phononic crystals. *Mechanics of Adv. Mater. and Struc.* **2020**, 27, 1053-1064.

21. B. Ash, A. Rezk, L. Yeo, G. Nash, Subwavelength confinement of propagating surface acoustic waves. *Appl. Phys. Lett.* **2021**, 118, 013502.

22. Z.-D. Zhang, F.-K. Liu, S.-Y. Yu, M.-H. Lu, Y.-F. Chen, An integrable and configurable phononic beam splitter based on self-collimated surface acoustic waves. *Appl. Phys. Express.* **2020**, 13, 044002.

23. P. Wang, L. Lu, K. Bertoldi, Topological phononic crystals with one-way elastic edge waves. *Phys. Rev. Lett.* **2015**, 115, 104302.

24. Y. Liu, X. Chen, Y. Xu, Topological Phononics: From Fundamental Models to Real Materials. *Adv. Funct. Mater.* **2020**, 30, 1904784.

25. P. H. Otsuka, K. Nanri, O. Matsuda, M. Tomoda, D. Profunser, I. Veres *et al.*, Broadband evolution of phononic-crystal-waveguide eigenstates in real-and k-spaces. *Sci. Rep.* **2013**, 3, 1-5.

26. S. Benchabane, O. Gaiffe, R. Salut, G. Ulliac, V. Laude, K. Kokkonen, Guidance of surface waves in a micron-scale phononic crystal line-defect waveguide. *Appl. Phys. Lett.* **2015**, 106, 081903.

27. D. Hatanaka, H. Yamaguchi, Real-space characterization of cavity-coupled waveguide systems in hypersonic phononic crystals. *Phys. Rev. Appl.* **2020**, 13, 024005.

28. Y. Guo, M. I. N. Rosa, M. Gupta, B. E. Dolan, B. Fields, L. Valdevit *et al.*, Minimal Surface‐Based Materials for Topological Elastic Wave Guiding. *Adv. Funct. Mater.* **2022**, 2204122.

29. Y. D. Dahmani, C. J. Sarabalis, W. Jiang, F. M. Mayor, A. H. Safavi-Naeini, Piezoelectric transduction of a wavelength-scale mechanical waveguide. *Phys. Rev. Appl.* **2020**, 13, 024069.

30. Y.-F. Wang, T.-T. Wang, J.-P. Liu, Y.-S. Wang, V. Laude, Guiding and splitting Lamb waves in coupled-resonator elastic waveguides. *Compo. Struc.* **2018**, 206, 588-593.

31. W. Fu, Z. Shen, Y. Xu, C.-L. Zou, R. Cheng, X. Han *et al.*, Phononic integrated circuitry and spin–orbit interaction of phonons. *Nat. Commun.* **2019**, 10, 1-7.

32. J.-Q. Wang, Z.-D. Zhang, S.-Y. Yu, H. Ge, K.-F. Liu, T. Wu *et al.*, Extended topological valley-locked surface acoustic waves. *Nat. Commun.* **2022**, 13, 1-8.

33. C. Pouya, G. R. Nash, Sub-and supersonic elastic waves in an annular hole phononic metamaterial. *Commun. Mater.* **2021**, 2, 1-8.

34. C. W. Hsu, B. Zhen, A. D. Stone, J. D. Joannopoulos, M. Soljačić, Bound states in the continuum. *Nature Reviews Materials* **2016**, 1, 1-13.

35. L. Shao, D. Zhu, M. Colangelo, D. Lee, N. Sinclair, Y. Hu *et al.*, Electrical control of surface acoustic waves. *Nature Electronics* **2022**, 1-8.